Frequency Stabilization of Nanomechanical Resonators Using Thermally Invariant Strain Engineering

Mingkang Wang[2,3,‡], *Rui Zhang*[1,‡], *Robert Ilic*[2], *Vladimir Aksyuk*[2,*], *and Yuxiang Liu*[1,**]

[1]Department of Mechanical Engineering, Worcester Polytechnic Institute, Worcester, MA 011609 USA

[2]Microsystems and Nanotechnology Division, National Institute of Standards and Technology, Gaithersburg, MD 20899 USA

[3]Institute for Research in Electronics and Applied Physics, University of Maryland, College Park, MD 20742, USA

KEYWORDS: Frequency stabilization, temperature compensation, NEMs, strain engineering, optomechanical readout

ABSTRACT

Microfabricated mechanical resonators enable precision measurement techniques from atomic force microscopy to emerging quantum applications. The resonance frequency-based physical sensing combines high precision with long-term stability. However, widely-used Si_3N_4 resonators suffer from frequency sensitivity to temperature due to the differential thermal expansion vs. the Si substrates. Here we experimentally demonstrate temperature- and residual stress-insensitive 16.51 MHz tuning fork nanobeam resonators with nonlinear clamps defining the stress and

frequency by design, achieving low fractional frequency sensitivity of $(2.5 \pm 0.8)\times10^{-6}$ K^{-1}, a 72× reduction. On-chip optical readout of resonator thermomechanical fluctuations allows precision frequency measurement without any external excitation at the thermodynamically-limited frequency Allan deviation of ≈ 7 $Hz/Hz^{1/2}$ and (relative) bias stability of ≈ 10 Hz ($\approx 0.6\times10^{-6}$) above 1 s averaging, remarkably, on par with state-of-the-art driven devices of similar mass. Both the resonator stabilization and the passive frequency readout can benefit a wide variety of micromechanical sensors.

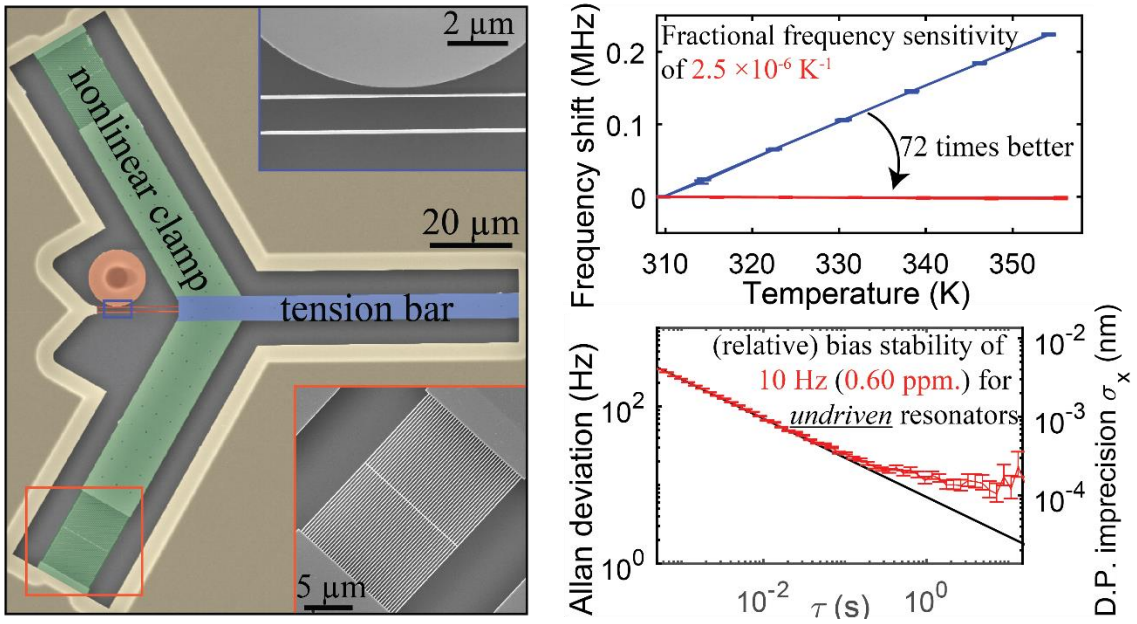

For Table of Contents Only

Mechanical instruments have been used as measurement tools for hundreds of years. With the advent of micro/nanofabrication, micro/nano−electro−mechanical systems (M/NEMS) have helped to advance our fundamental understanding of mesoscale physics and found a broad range of commercial applications, such as inertial sensing in automobiles and smartphones. While some of these sensors detect external forces or torques by converting them directly into mechanical

displacements, a widely-used high-performance alternative is to convert the unknown parameter, such as an added mass and a force or a torque gradient, into a change in the frequency of a high-quality factor mechanical resonator. This modality is the basis of frequency-modulated atomic force microscopy (FM-AFM)[1] and was used in a variety of demanding experiments operating in vacuum[2,3], air[4] or even liquid[5]. Frequency-based sensing provides a high measurement accuracy, dynamic range and sensitivity with stability over a long averaging time, all of which are determined by the high-quality mechanical system, while being immune to the nonlinearity, low-frequency noise, and gain and bias drift in the electro- or opto-mechanical displacement detection.

In most of the cases, high frequency – quality factor (fQ) products are beneficial for frequency-modulated schemes. Increasing the resonance frequency enables higher dynamic range, while lowering the dissipation and associated thermodynamic Langevin force noise power improves the fundamental limits on the frequency measurement uncertainty for a given excitation force. Nanomechanical resonators made of high intrinsic tensile stress silicon nitride (Si_3N_4) have shown great potential for such sensing applications[6] because of their high mechanical quality factors, high frequencies, and facile fabrication. Stress engineering has been applied to increase fQ products of nanoscale Si_3N_4 tuning forks[7] and has been recently combined with dissipation-dilution to achieve breakthrough improvements in fQ, reaching 10^{14} to 10^{15} range[8,9], sufficient in principle to observe quantum-mechanical behavior at room temperature.

These advances open exciting opportunities for on-chip motion metrology and sensing. However, the frequency of such devices is determined by both designed geometry and the intrinsic stress (σ_0). Unfortunately, σ_0 varies with different fabrication processes[10]. Additionally, the frequency of the mode of interest in the conventional stress-engineered doubly-clamped or drum-head design geometries is strongly influenced by temperature due to the difference of the

coefficient of thermal expansion (CTE) between the Si_3N_4 device layer and the Si substrate most commonly used for such devices. The differential Si - Si_3N_4 CTE results in a strong temperature dependence of the Si_3N_4 stress for rigidly clamped spatially-extended device[11]. Therefore any uncontrolled temperature changes induce undesirable frequency fluctuations[12], requiring differential sensing schemes. The majority of current technical approaches for compensating temperature-induced frequency variation rely on matching different materials[13] or active temperature control[14].

In this study, we show that doubly-clamped tensile mechanical resonators can be made insensitive to residual stress and temperature variation by using a completely passive stress-engineered clamp co-fabricated from the same planar tensile-stress film. The clamp is designed to apply a predetermined amount of stress (exceeding the residual stress of the film, if desired), and maintain the resonator stress irrespective of the value of the residual stress or its thermally-induced variation due to the differential CTE. The experimentally measured frequency sensitivity to temperature of nanoscale Si_3N_4 tuning forks is lowered from 5050 Hz/K ± 40 Hz/K with $f_m \approx 27.76$ MHz for a reference uncompensated fork to -42 Hz/K ± 14 Hz/K at $f_m \approx 16.51$ MHz for a tuning fork with the compensating clamp, achieving a fractional frequency sensitivity of $(2.5 \pm 0.8)\cdot 10^{-6}$ K^{-1}, an ≈ 72 times reduction. All reported statistical uncertainties are one standard deviation over multiple measurements unless otherwise noted. Remarkably, we measure low frequency Allan deviation $\sigma_f \approx 10$ Hz ($\frac{\sigma_f}{f_m} \approx 0.60\times 10^{-6}$) for ≥ 1 s averaging without any applied drive force, by only detecting the motion of the thermodynamically fluctuating mechanical resonator with a sensitive integrated cavity optomechanical readout. The measured resonator line width of ≈ 600 Hz, the measured Allan deviation slope and bias stability are shown to be unaffected by the temperature-compensating clamping mechanism.

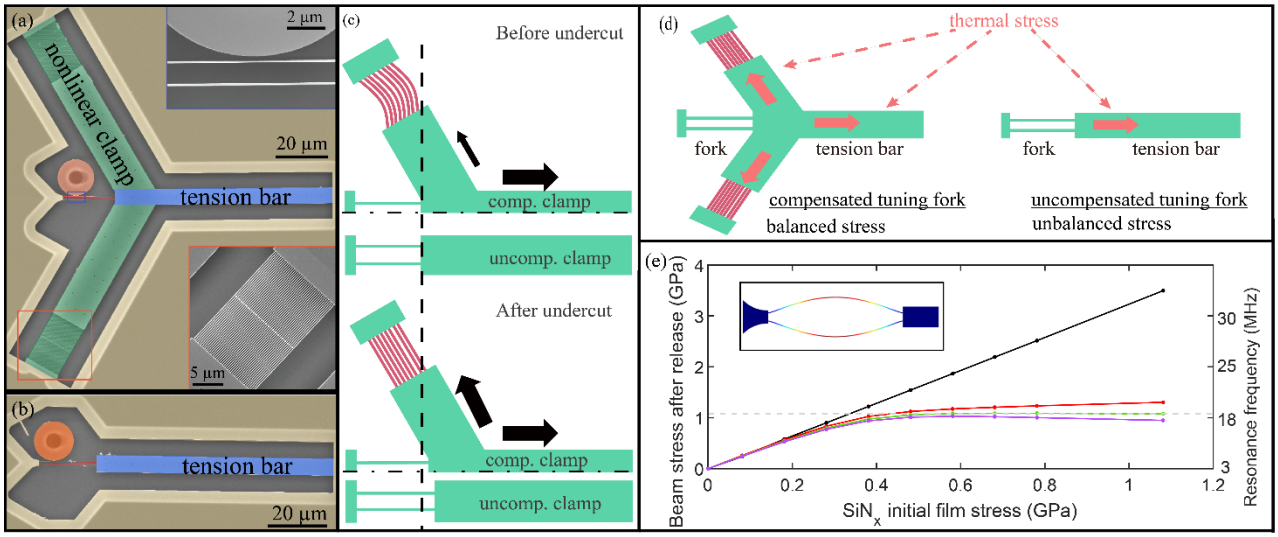

Figure 1. False-color electron micrographs of a tuning fork (a) with and (b) without temperature compensation. Bottom inset: Straightened nonlinear springs. Top inset: integrated photonic readout – microdisk optical resonator evanescently coupled to a tuning fork nanobeam. (c) Working principle of stress tuning during release. The schematic of the symmetric compensated device is shown as half. Before undercut, the nonlinear clamps provide less residual stress due to the curved springs. After undercut, the springs are fully stretched, providing stress equal to the stress of tension bar. (d) Working principle of temperature compensation after release. For optimally compensated devices, the extra stress of clamps and tension bar cancel each other, resulting in a temperature insensitive fork. (e) Numerical simulation of tuning fork beam stress and frequency vs. Si_3N_4 film initial (residual) stress. Different clamp geometries produce positive (red), neutral (green) and negative (purple) residual stress dependence above the threshold residual stress value of ≈ 0.4 GPa. Inset: The simulated tuning fork in-plane squeezing mode shape with exaggerated deformation.

Scanning electron microscopy (SEM) images of temperature compensated and uncompensated tuning forks are shown in Figures 1(a) and (b), respectively. Each device consists of a tuning fork mechanical resonator and a microdisk optical resonator for near-field optical

readout of the tuning fork mechanical motion[7]. The uncompensated tuning fork consists of two parallel cantilever beams, and is doubly clamped with a long tension bar on the right. By comparison, the compensated tuning fork has two additional inclined-clamp bars, resulting in a Y-shaped clamp at the right end of the tuning fork. Each of the inclined clamps is attached to the supporting structure by an array of geometrically nonlinear springs. All the devices are fabricated in a 250 nm thick stoichiometric Si_3N_4 layer, which is grown by low-pressure chemical vapor deposition (LPCVD) on a 3 μm thick silicon dioxide (SiO_2) layer on a silicon substrate. We first used electron-beam (E-beam) lithography to define the geometry in a layer of positive tone E-beam resist. The pattern was then transferred to the Si_3N_4 film by a $CHF_3/Ar/O_2$ inductively-coupled plasma reactive ion etch (ICP RIE). Device fabrication is finished by a buffered oxide etch (BOE) undercut, which selectively removes the SiO_2 to release the device with minimal etching of Si_3N_4.

The nominal length and width of the tuning fork beams are 20 μm and 150 nm, respectively, in all the fabricated devices. The tension bar on the right-hand side of the tuning fork is 80 μm long. In the uncompensated device, the tension bar shrinks after device release due to the redistribution of the initially uniform Si_3N_4 stress, such that the stress in the tuning fork beam increases, as shown in Figure 1(c). Because the length of the tension bar determines the final stress in the tuning fork after undercut, one can tune the fork mechanical frequency simply by the design of the tension bar. This design-enabled tuning has been demonstrated in our previous work to achieve an up-to-three-fold stress increase, compared with the intrinsic Si_3N_4 film stress[7]

In the temperature-compensated device (shown in Figure 1(a)), the Y-shaped clamp includes two symmetric clamp beams inclined $\pm 120°$ relative to the tension bar. Opposite the bar, each clamp beam is connected to the frame and the substrate via an array of 22 geometrically

nonlinear springs. The springs are curved before undercut with the shape defined by one period of a cosine function as $A_0\cos(2\pi x/L)$, where A_0 = 0.48 μm is the amplitude of the cosine geometry, L = 20 μm is the length of the springs and x is the position along the longitudinal direction. They are designed to greatly and abruptly increase in stiffness at a strain value predetermined by the shape parameters A_0 and L. This is achieved by choosing a curve that is as smooth as possible and choosing the narrowest width we can confidently fabricate for each curved beam to minimize initial stiffness. For the cosine shape, the total length along the beam is approximately $L + \pi^2 \frac{{A_0}^2}{L}$, therefore the transition is occurring at the nominal displacement of approximately $\pi^2 \frac{{A_0}^2}{L}$ = 0.11 μm (Supplementary Information). The ratio of the combined width of the nonlinear springs to the tension bar width affects the balancing point after release and the temperature response of the tuning fork.

These additional inclined-clamps and the curved springs allow the tuning fork beam stress to be insensitive to the intrinsic Si_3N_4 stress while retaining the stress tuning capability enabled by the tension bar. During the release process (upper panel of Figure 1(c)), the tension bar first shrinks, as in the uncompensated device, stretching the tuning fork beams and straightening the curved springs in the inclined clamps. As a result, the tension bar increases the tuning fork beam stress and frequency similar to that in the uncompensated device. However, when the intrinsic Si_3N_4 film stress is large enough to fully straighten the nonlinear springs, their stiffness increases. The symmetric, inclined clamps then provide an effective balancing force in the opposite direction of the stretching force produced by the tension bar (lower panel of Figure 1(c)). Depending on the width of the elements, with the further increase in the residual stress the right-hand end-point of the compensated tuning fork can be designed to move left, right or stay fixed relative to the left-hand end-point. Hence the tuning fork beam stress as well as mechanical frequency can be

determined by the design geometry insensitive to the initial, residual Si_3N_4 film stress. Thanks to the nonlinear temperature compensation clamps, the stretched tuning fork not only benefits from the stress-tuning-induced high frequency-quality factor product, but also becomes independent from the intrinsic stress and the ambient temperature variations.

The stress insensitivity of the frequency enabled by the clamp design is illustrated by the results of Finite-Element-Method (FEM) simulations for typical clamp geometries. Figure 1(e) depicts the modeled final beam stresses and mechanical frequencies of devices with different compensation level for different Si_3N_4 initial film stress. In the uncompensated device, the beam stress is linearly proportional to the intrinsic stress, $\sigma \approx 3.3\ \sigma_0$. In the compensated device, the beam stress in the tuning fork increases similarly for small intrinsic stress, before the nonlinear springs are fully straightened. When the intrinsic stress is above the threshold value (≈ 0.4 GPa) at which the nonlinear springs become straight and stiff, the beam stress becomes much less sensitive to the change of intrinsic stress as the inclined clamp beams counter-balance the tension bar. Note that the ≈ 1 GPa 'clamped' stress value (and the corresponding 'clamped' frequency) is below that of the uncompensated device. However, the compensated device beam stress still significantly exceeds the residual stress for most of the horizontal axis range in the figure, thus the stress engineering ability is retained.

By changing the width ratio between the tension bar to the nonlinear spring, we can manipulate the balancing and the response of tuning forks to temperature. As a result, large, optimal, and small ratios of tension bar to nonlinear spring width produce under-compensated, optimally compensated, and over-compensated tuning forks, respectively. In Figure 1(e), the under (red), optimal (green), and over (purple) compensation in the simulation are achieved by fixing the

nonlinear spring width to 180 nm and varying the tension bar width to be 4 μm, 3.4 μm, and 3.1 μm, respectively. Note that in the optimally-compensated device, the beam stress is almost constant after the nonlinear springs become fully straightened: the final beam stress in this device is determined by the clamp geometry only (the threshold displacement required to straighten the nonlinear spring) and is insensitive to the exact value of the Si_3N_4 intrinsic film stress.

The stress and frequency variations due to differential CTE are equivalent to variation due to the change in the residual stress: in a device prior to release the thermal expansion of the substrate results in a change in the thin film stress with a change in temperature. As illustrated in Figure 1(d), the optimally balanced Y clamp can be designed to maintain the constant strain of the

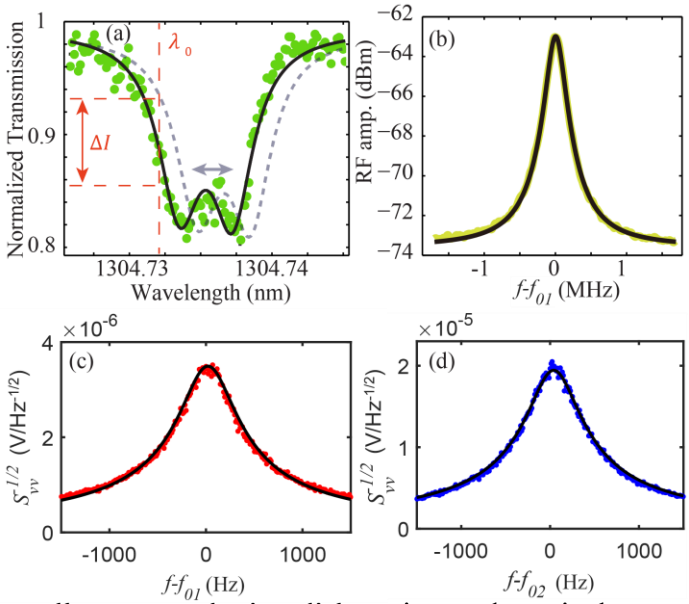

Figure 2. (a) Experimentally measured microdisk cavity mode optical spectrum with quality factor of 5.30×10^5. During the measurement, the laser wavelength (λ_0) is fixed on the shoulder of the degenerate optical modes. The motion of the fork modulates the resonance of the optical mode, inducing varying transmission intensity proportional to the relative position of the fork. (b) mechanical vibration power spectral density for the compensated fork in air. (c),(d) mechanical spectra, in vacuum, of the compensated and uncompensated devices, respectively. Black solid lines are theoretical fit.

tuning fork despite such differential thermal expansion of the nitride film relative to the Si substrate. Note that for resonator film materials with significant variation of the Youngs modulus with temperature the clamp can be modified to compensate for the linear part of such variation, maintaining constant nanoresonator stress rather than strain. However, this comes at the expense of non-zero sensitivity to the initial residual stress in the film.

While the described stress control approach relies on a tensile initial residual stress, the resulting temperature-insensitive stress in the resonator may be engineered to be compressive as well as tensile, if desired. To achieve this reversal, the nonlinear clamps would be replaced by tension bars while the tension bar would be replaced by an appropriately sized nonlinear clamp including nonlinear springs. This arrangement may help achieve and maintain a tensile stress lower than the initial stress, a zero stress or a compressive stress in the tuning fork. The idea may be applied to devices such as buckled beams memory units[15].

To experimentally validate the approach, we have investigated the temperature dependence of fork frequency for designs with a varying ratio between the nonlinear spring and the tension bar widths. We have fabricated and tested devices with the nominal tension bar width varying from 2.9 μm to 3.4 μm and nonlinear spring widths varied from 170 nm to 245 nm.

The mechanical frequencies of the tuning forks are measured through a near-field cavity-optomechanical readout[16]. Each tuning fork is near-field coupled across a ≈ 150 nm gap to a Si_3N_4 microdisk optical cavity. The disk has a nominal diameter of 14 μm and supports whispering-gallery (WGM) optical modes (Figure 2(a)). The tuning fork beam motion shifts the optical mode center frequency. When the interrogation laser is tuned to the shoulder of the optical resonance near the point of the highest slope, the transmitted optical intensity is modulated proportional to the mechanical displacement. The optomechanical coupling parameter $g_{om}/2\pi$ between the tuning

fork in-plane squeezing mechanical mode and the microdisk WGM is calculated to be ≈ 140 MHz/nm, which indicates the optical mode frequency shift per unit modal displacement of the mechanical resonator. This near-field optical readout yields ≈ 1 fm/Hz$^{1/2}$ displacement resolution[16] and enables a monolithic, robust, and fiber-pigtailed sensor technology[17].

To measure the mechanical frequencies, light was emitted from a 1300 nm wavelength band tunable laser and evanescently coupled to the optical microdisk resonator through a fiber taper helix probe[18]. The transmitted light intensity was measured by a photodetector (PD), with the output split into two channels. One channel connected to a data acquisition (DAQ) board for swept-wavelength spectroscopy of the optical cavity modes (Figure 2(a)). The other channel connected to an Electrical Spectrum Analyzer (ESA) to measure the mechanical power spectral density in air (Figure 2(b)) and extract the resonance frequency. In the subsequent tests of the frequency stability, the devices were placed in a vacuum chamber and a lock-in amplifier was used to capture time-domain mechanical motion, with root mean square of power spectral densities shown in Figure 2(c,d).

Since the optomechanical transduction noise is well below the random motion of the tuning fork driven by thermomechanical noise[7,19], the mechanical frequencies were measured from the thermal motion spectra of the tuning forks without external excitation. The temperature was stably controlled within ± 0.1 K by a ceramic heater with a proportional–integral–derivative (PID) controller. The device was enclosed inside an acrylic chamber, with desiccant boxes placed in the chamber and constant desiccated air flowing through the chamber, to minimize the influence from moisture on the devices. At room temperature the frequencies of the first-order squeezing mode

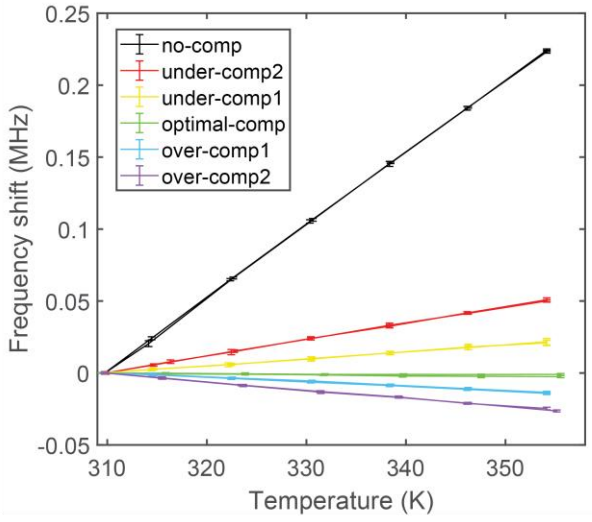

	nlin. W(μm)	t.bar W(μm)	t.bar W/nlin. W	slope (Hz/K)	slope uncert.(Hz/K)
no-comp	-	3.20	-	5050	40
under-comp2	0.17	3.42	20.12	1136	14
under-comp1	0.161	2.91	18.07	481	12
optimal-comp	0.184	2.96	16.09	-42	14
over-comp1	0.204	2.98	14.61	-315	15
over-comp2	0.245	3.2	13.06	-563	18

Figure 3. Experimentally measured temperature-induced frequency shift. The lines of the slopes from large to small corresponds to uncompensated devices to over-compensated devices. As the temperature is swept up and down, no large hysteresis shows on any line. The one standard deviation statistical uncertainties for the temperature sensitivity are determined by the linear least squares fits. The table shows the values of device parameters and temperature sensitivities.

were $f_{01} \approx 16.51$ MHz and $f_{02} \approx 27.76$ MHz for the compensated and uncompensated tuning forks, respectively.

To verify the temperature compensation effect, the mechanical frequency shifts of different devices over the temperature range between 308 K (35 °C) and 355 K (82 °C) were measured as shown in Figure 3. Each measurement includes a downward followed by an upward temperature sweep and minimum hysteresis was found during the experiment. The table shows the designed values of nonlinear spring width (nlin. W), tension bar width (t.bar W), tension bar to nonlinear spring width ratio (t.bar W/nlin. W), measured temperature sensitivities (slope), and temperature sensitivity slope uncertainties (slope uncert.) for all the measured devices.

The resonant frequency of the uncompensated device increased linearly with temperature at the rate of 5050 Hz/K ± 40 Hz/K. For a beam vibration dominated by the tensile stress, the fundamental mode resonant frequency f_m as a function of temperature T can be described as[12]:

$$f_m(T) = \frac{1}{2L}\sqrt{\frac{\sigma(T_0) - AE(\alpha_{beam} - \alpha_{sub})(T - T_0)}{\rho}} \quad (1)$$

where L is the beam length, $\sigma(T_0)$ is the tensile stress along the beam at reference temperature T_0, ρ is the density of the beam, E is the Young's modulus of the beam material, and α_{beam} and α_{sub} are the CTE of the beam and substrate, respectively. Note that for the tuning fork with a tension bar, the stress is amplified relative to the residual stress σ_o by an amplification ratio $A = \sigma(T_0)/\sigma_o$ and the stress variation due to differential CTE is similarly amplified.

Since the CTE of the Si substrate ($\approx 2.6\times10^{-6}$ K^{-1}) is larger than that of Si_3N_4 device layer ($\approx 1.6\cdot10^{-6}$ K^{-1}), the f_m increases as temperature increases. For uncompensated device $\sigma(T_0) \approx 1.81$ GPa (calculated by FEM) is large relative to the thermal variation, and therefore we need to consider only the linear term: the temperature sensitivity can be then calculated as

$$S = \frac{\partial f_m}{\partial T}\Big|_{T=T_0} = -\frac{AE(\alpha_{beam} - \alpha_{sub})}{4L\sqrt{\rho\sigma(T_0)}} \quad (2)$$

By using FEM-calculated values of $A \approx 3.12$, $E \approx 310$ GPa and $\rho \approx 3000$ kg/m^3 for the Si_3N_4 film, the uncompensated fork temperature sensitivity is calculated to be ≈ 5200 Hz/K, which also matches the experiment.

For compensated devices, the resonant frequencies are also linearly-proportional to the temperature change but with much lower temperature sensitivity. Given the measured frequency of the uncompensated device, the residual stress is well above the threshold and the nonlinear springs are fully deployed as designed. Five temperature compensation strengths are experimentally demonstrated using different tension-bar to nonlinear spring width ratios. As shown in Figure 3 and the table, the frequency variation with temperature decreases, crosses zero and becomes negative with decreasing of tension bar to nonlinear spring ratio, illustrating engineering the temperature sensitivity by geometry design. The minimum temperature sensitivity of -42 Hz/K ± 14 Hz/K (fractional frequency sensitivity of (2.5 ± 0.8)·10^{-6} K^{-1}) is measured. Comparing to the uncompensated tuning fork, which has 5050 Hz/K ± 400 Hz/K (fractional sensitivity (182 ± 1)·10^{-6} K^{-1}), the temperature sensitivity is reduced by a factor of ≈ 72 using the passive temperature compensation design. In all cases, the temperature sensitivity is independent of temperature over the experimental temperature range of ≈ 50 K.

Such tuning forks can be used as frequency-readout displacement sensors in larger microsystems. For example, the compensating Y clamp can be anchored to the stationary substrate, while the left-hand side of the tuning fork can be attached to a larger, 100 μm or millimeter-scale movable proof mass of a micromachined accelerometer. The fork resonator frequency will change proportional to the proof mass displacement, providing a sensitive, stable and high dynamic range motion readout. Although our devices have not yet been tested directly as mechanical motion sensors, the displacement sensitivity of the resonance frequency is numerically and analytically estimated to be ≈ 51 kHz/nm for the uncompensated fork and ≈ 74 kHz/nm for the compensated fork based on the device dimension and resonant frequency measured in the experiments. Therefore, we have further investigated the frequency noise and stability (and the corresponding achievable displacement readout noise and stability) for our devices and any effects the compensating Y clamp may have on these performance parameters. The measurements are performed in vacuum to lower the resonator dissipation rate by eliminating air damping to improve the thermodynamically-limited frequency measurement uncertainty.

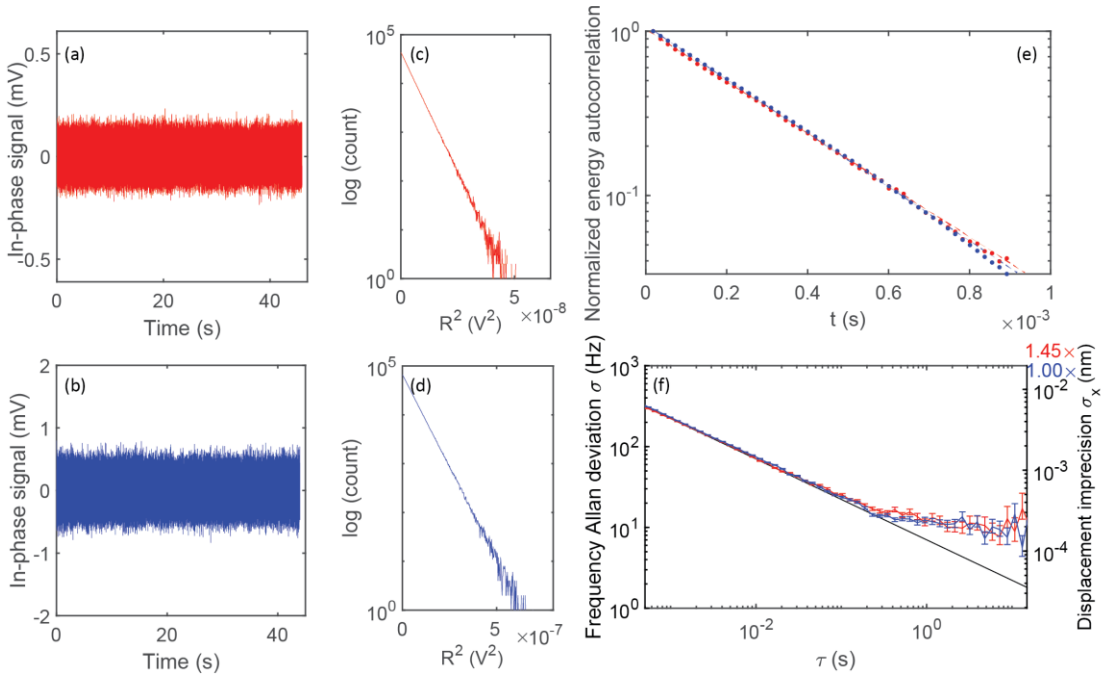

Figure 4. Time domain in-phase component of thermal mechanical vibration signal for (a) compensated and (b) uncompensated tuning forks. Boltzmann-distributed square of the vibration amplitude for (c) compensated and (d) uncompensated resonator. (e) Normalized energy autocorrelation calculated from time domain signal of the compensated (red) and uncompensated (blue) device. Red (blue) dash line is corresponding exponential fit for the compensated (uncompensated) device. Compensated and uncompensated decay times are similar and agree with the resonance line widths. Error bars are comparable with the size of dots. (f). Experimentally measured frequency Allan deviation for compensated and uncompensated tuning forks driven solely by thermal fluctuations, without external excitation. Right-hand-side axis shows the corresponding achievable displacement imprecision when used as an on-chip displacement sensor. Different calculated frequency sensitivities to displacement for compensated and uncompensated devices result in different scale multipliers: 1.00× (uncompensated) and 1.45× (compensated). The uncertainties for Allan deviation are determined by Chi-Squared Confidence Intervals[23].

Fig. 4 (a), (b) show the in-phase component of the lockin-detected mechanical displacement signal of the optimally compensated (Dev1) and the uncompensated (Dev2) device, respectively. No driving forces are applied and the devices are only subject to thermodynamic fluctuations at room temperature. The corresponding response in the frequency domain is shown in Fig. 2 (c), (d), where the Lorentz fit gives the mechanical damping of Dev1 and Dev2, $\Gamma_{D1}/2\pi = (604.7 \pm 9.3)$ Hz and $\Gamma_{D2}/2\pi = (630.1 \pm 15.6)$ Hz, respectively. Fig, 4 (c), (d) present the distribution of the time-domain signal amplitude squared R^2, which is a straight line in log scale indicating that, as expected, the energy obeys the Maxwell-Boltzmann distribution ($\propto \exp[-\alpha R^2/(2k_BT)]$), where k_B is the Boltzmann constant and α is a constant determined by the readout

gain, illustrating readout linearity. Fig. 4 (e) shows that the energy autocorrelation, $\langle R^2(t_0)R^2(t_0+t)\rangle - \langle R^2(t)\rangle^2$ of Dev1 and Dev2 in log scale is a linear function of t. Linear fits of the autocorrelations show that the energy relaxation time of the Dev1 and Dev2 are $T_{1,\mathrm{D1}} = 0.270\ \mathrm{ms} \pm 0.004\ \mathrm{ms}$ and $T_{1,\mathrm{D2}} = 0.257\ \mathrm{ms} \pm 0.003\ \mathrm{ms}$, showing an energy dissipation rate of $\Gamma_{0,\mathrm{D1}}/2\pi = 590.2\ \mathrm{Hz} \pm 8.5\ \mathrm{Hz}$ and $\Gamma_{0,\mathrm{D2}}/2\pi = 620.3\ \mathrm{Hz} \pm 7.8\ \mathrm{Hz}$. These values are close to the damping rates obtained from the fits to the spectra in Figure 2, indicating that the devices are not subject to much dephasing. In addition, the mechanical damping of both devices are approximately equal, showing that the Y-shape compensation structures do not add much extra dissipation to the system.

The precision of these devices as frequency-based sensors depends on their frequency stability and our ability to precisely measure their frequency. While typically such sensors are driven to a large amplitude in order to lower the frequency measurement imprecision[20], here we extract the frequency from the time-domain signal of thermal mechanical motion, precisely measured with the integrated cavity optomechanical readout. Its Allan deviation, shown in Figure 4 (f), illustrates that the uncertainly of such frequency measurement can be remarkably low, useful for practical applications. The data for averaging times below 0.1 s agrees precisely with the thermodynamic frequency uncertainty limit (Cramer-Rao lower bound) for undriven resonator subject to thermal noise[21]:

$$CRLB(f) = \frac{1}{2\pi}\sqrt{\frac{\Gamma}{2\tau}} \tag{3}$$

where τ is length of averaging time for the Allan deviation and the $\Gamma/2\pi$ = 620 Hz is used, based on the measured values.

In the experiment, the frequency $f(t)$ is calculated from phase difference between each two adjacent lockin data points[22]:

$$f_i(t) = \frac{\varphi_{i+1} - \varphi_i}{2\pi\ dt} = \frac{x_{i+1} - x_i}{2\pi\ dt\ |x_i|} \tag{4}$$

where φ_i is the phase of a complex-valued lockin data sample x_i, and $dt \ll 1/\Gamma$ represents the sampling interval. Subject to thermal diffusion during the short time dt, the variance ${\sigma_{\mathrm{d}t}}^2$ of $x_{i+1} - x_i$ is a constant. Therefore, for a sample x_i, the estimated frequency, $f_i(t)$ has a variance proportional to $1/|x_i|^2$, i.e. the frequency estimation is more certain for samples with larger amplitude. Given a series of $f_i(t)$ over the *n*-th time interval of length τ the best estimate of the frequency from that time interval is the inverse-variance-weighted average:

$$\overline{f_{n\tau}}(\tau) = \frac{\langle |x_i|^2 f_i(t) \rangle_{n\tau}}{\langle |x_i|^2 \rangle_{n\tau}} \tag{5}$$

where $\langle \dots \rangle_{n\tau}$ represents average of the data in a time interval $[(n-1)\tau, n\tau]$.

Similarly, we calculate the Allan variance as a weighted average:

$$\sigma_\tau^2(\tau) = \frac{1}{2} \langle W_{n\tau}^2 \left[\overline{f_{(n+1)\tau}}(\tau) - \overline{f_{n\tau}}(\tau) \right]^2 \rangle_{T_0} \tag{6}$$

where $\langle \dots \rangle_{T_0}$ represents average of the data over the full-time trace of length T_0 and $W_{n\tau}$ represents the weight of each element. The weights are $W_{n\tau} = \langle |x_i|^2 \rangle_{n\tau} / \langle |x_i|^2 \rangle_{T_0}$ and tend to conventional unity weights for the $\tau > 1/\Gamma$, while deviating from unity at small τ. Although there is no significant difference between weighted and unweighted Allan deviation for $\tau > 1/\Gamma$, for short time scales the widely used unweighted Allan deviation is only appropriate for driven resonators, where $W_{n\tau} \approx 1$ on all time scales.

Fig.4 (f) shows the Allan deviation of the two devices. At $\tau \lesssim 100$ ms, the frequency stability reaches the thermodynamic limit for resonators without drive. Note that this undriven limit is easier to reach compared to the thermodynamic limit under maximum drive still producing

linear response[19,20]. At $\tau \gtrsim 100$ ms, the Allan deviation is above the thermodynamic limit, indicative of a long-term frequency fluctuation process, such as commonly observed in many nanomechanical devices[19,20]. Both devices present similar bias stability of ≈ 10 Hz at τ of ≈ 1 s to 10 s. The temperature compensation is achieved without degrading frequency noise and stability compared to the uncompensated control device. The ability to measure the relative frequency stability of $\approx 0.60\times10^{-6}$ in 1 s bandwidth for the compensated device without any applied drive force is noteworthy, being on par with state-of-the-art driven devices of similar mass[19]. Finally, given the modeled sensitivity to displacement, this corresponds to the ≈ 200 fm displacement imprecision for a 1 s measurement.

We have demonstrated a passive way to maintain the pre-defined tensile stress and resonance frequency in doubly-clamped nanofabricated mechanical resonators over a broad range of initial tensile material stress and operating temperature, regardless of the CTE mismatch with the substrate. This is achieved by attaching the resonator at one end to a special stress-engineered nonlinear compensating clamp, co-fabricated from the same tensile film. A broadly-used Si_3N_4 on Si nanofabrication platform is used to demonstrate stabilizing a ≈ 16.51 MHz, high-Q nanoscale tuning fork resonator, reducing its relative frequency temperature sensitivity by ≈ 72 times, down to $(2.5 \pm 0.8)\cdot10^{-6}$ K^{-1} at room temperature. Using a sensitive integrated cavity optomechanical readout to passively detect the motion of undriven, thermodynamically fluctuating resonator, we show that the frequency uncertainty remains at the thermodynamic limit of ≈ 7 $Hz/Hz^{1/2}$ for up to 0.1 s averaging, and the frequency (relative) bias stability is ≈ 10 Hz ($\approx 0.60\times10^{-6}$) above 1 s averaging. Importantly, the resonator dissipation rate, frequency noise and bias stability are unaffected by the stress stabilization and temperature compensation mechanism. This universal nonlinear clamp approach can be directly integrated with various existing tensile MEMS/NEMS

resonators for temperature/stress compensation. Additionally, the described temperature-compensated resonant transducer, operable without external drive, introduces a novel approach for practical, high-precision, low-drift on-chip displacement measurement for MEMS sensor applications.

Corresponding Author

* Email: vladimir.aksyuk@nist.gov

** Email: yliu11@WPI.EDU

Author contributions

V.A. conceived of the frequency stabilization approach and initial device design. R.Z., V.A. and Y.L. created device design and layout and conducted device modeling. R.Z., R.I. and Y.L. developed the fabrication process and fabricated the devices. R.Z. and Y.L. conducted the experiments and analyzed temperature dependence data. M.W. and V.A. developed frequency stability analysis and M.W. analyzed the data. M.W., V.A. and Y.L. wrote the manuscript. ‡M. W. and R. Z. contributed equally to this work.

Note

The authors declare that they have no conflict of interest

Acknowledgments

The authors are grateful to Jason Gorman, Daniel Lopez, Marcelo Davanco and J. Alexander

Liddle for insightful comments and suggestions for manuscript improvement. M.W. is supported by the Cooperative Research Agreement between the University of Maryland and the National Institute of Standards and Technology Center for Nanoscale Science and Technology, Award 70NANB10H193, through the University of Maryland.

Supporting information

This material is available free of charge via the internet at http://pubs.acs.org.

Detailed numerical simulation method of stress and eigenfrequencies as a function of initial stress;

Analysis of nonlinear springs and a simplified model;

REFERENCES

1. Giessibl, F. J. & Bielefeldt, H. Physical interpretation of frequency-modulation atomic force microscopy. *Phys. Rev. B* **61**, 9968–9971 (2000).
2. Mohideen, U. & Roy, A. Precision measurement of the Casimir force from 0.1 to 0.9 μ m. *Physical Review Letters* **81**, 4549 (1998).
3. Bolle, C. A. *et al.* Observation of mesoscopic vortex physics using micromechanical oscillators. *Nature* **399**, 43–46 (1999).
4. Garrett, J. L., Somers, D. A. T., Sendgikoski, K. & Munday, J. N. Sensitivity and accuracy of Casimir force measurements in air. *Phys. Rev. A* **100**, 022508 (2019).
5. Sugihara, T., Hayashi, I., Onishi, H., Kimura, K. & Tamura, A. Sub-nanometer-resolution imaging of peptide nanotubes in water using frequency modulation atomic force microscopy. *Chemical Physics* **419**, 74–77 (2013).

6. Suhel, A., Hauer, B. D., Biswas, T. S., Beach, K. S. D. & Davis, J. P. Dissipation mechanisms in thermomechanically driven silicon nitride nanostrings. *Appl. Phys. Lett.* **100**, 173111 (2012).
7. Zhang, R. *et al.* Integrated tuning fork nanocavity optomechanical transducers with high fMQM product and stress-engineered frequency tuning. *Appl. Phys. Lett.* **107**, 131110 (2015).
8. Tsaturyan, Y., Barg, A., Polzik, E. S. & Schliesser, A. Ultracoherent nanomechanical resonators via soft clamping and dissipation dilution. *Nature Nanotechnology* **12**, 776–783 (2017).
9. Ghadimi, A. H. *et al.* Elastic strain engineering for ultralow mechanical dissipation. *Science* **360**, 764–768 (2018).
10. Temple-Boyer, P., Rossi, C., Saint-Etienne, E. & Scheid, E. Residual stress in low pressure chemical vapor deposition SiNx films deposited from silane and ammonia. *Journal of Vacuum Science & Technology A* **16**, 2003–2007 (1998).
11. Kose, T., Azgin, K. & Akin, T. Design and fabrication of a high performance resonant MEMS temperature sensor. *J. Micromech. Microeng.* **26**, 045012 (2016).
12. Larsen, T. *et al.* Ultrasensitive string-based temperature sensors. *Appl. Phys. Lett.* **98**, 121901 (2011).
13. Myers, D. R., Azevedo, R. G., Chen, L., Mehregany, M. & Pisano, A. P. Passive Substrate Temperature Compensation of Doubly Anchored Double-Ended Tuning Forks. *Journal of Microelectromechanical Systems* **21**, 1321–1328 (2012).

14. Salvia, J. C., Melamud, R., Chandorkar, S. A., Lord, S. F. & Kenny, T. W. Real-Time Temperature Compensation of MEMS Oscillators Using an Integrated Micro-Oven and a Phase-Locked Loop. *Journal of Microelectromechanical Systems* **19**, 192–201 (2010).
15. Bagheri, M., Poot, M., Li, M., Pernice, W. P. H. & Tang, H. X. Dynamic manipulation of nanomechanical resonators in the high-amplitude regime and non-volatile mechanical memory operation. *Nature Nanotechnology* **6**, 726–732 (2011).
16. Liu, Y., Miao, H., Aksyuk, V. & Srinivasan, K. Wide cantilever stiffness range cavity optomechanical sensors for atomic force microscopy. *Opt. Express, OE* **20**, 18268–18280 (2012).
17. Chae, J. *et al.* Nanophotonic Atomic Force Microscope Transducers Enable Chemical Composition and Thermal Conductivity Measurements at the Nanoscale. *Nano Letters* **17**, 5587–5594 (2017).
18. Ren, Y., Zhang, R., Ti, C. & Liu, Y. Tapered optical fiber loops and helices for integrated photonic device characterization and microfluidic roller coasters. *Optica, OPTICA* **3**, 1205–1208 (2016).
19. Sansa, M. *et al.* Frequency fluctuations in silicon nanoresonators. *Nature Nanotech* **11**, 552–558 (2016).
20. Gavartin, E., Verlot, P. & Kippenberg, T. J. Stabilization of a linear nanomechanical oscillator to its thermodynamic limit. *Nat Commun* **4**, 2860 (2013).
21. Wang, M. & Aksyuk, V. Thermodynamic Limit for Linear Harmonic Oscillator Resonance Frequency Measurement. *arXiv:2001.10612 [physics]* (2019).
22. Kay, S. A fast and accurate single frequency estimator. *IEEE Trans. Acoustics, Speech, and Signal Processing* **37**, 1987–1990 (1989).

23. D.A. Howe, D.W. Allan and J.A. Barnes, Properties of Signal Sources and Measurement Methods, Proc. 35th Annu. Symp. on Freq. Contrl., pp. 1-47, May 1981.

Frequency Stabilization of Nanomechanical Resonators Using Thermally Invariant Strain Engineering

Mingkang Wang[2,3], Rui Zhang[1], Robert Ilic[2], Vladimir Aksyuk[2,], and Yuxiang Liu[1,**]*

[1]Department of Mechanical Engineering, Worcester Polytechnic Institute, Worcester, MA 011609 USA

[2]Microsystems and Nanotechnology Division, National Institute of Standards and Technology, Gaithersburg, MD 20899 USA

[3]Institute for Research in Electronics and Applied Physics, University of Maryland, College Park, MD 20742, USA

Corresponding Author

* Email: vladimir.aksyuk@nist.gov

** Email: yliu11@WPI.EDU

Finite-element-method numerical simulation of beam stress and eigenfrequency VS initial beam stress

The finite-element-method (FEM) is done on commercial software. The geometry parameters used in the simulation are the same as the nominal dimensions listed in the main text, for example, the size of the tuning fork is 20 μm long, 150 nm wide and 250 nm thick. Figure S1 shows the top view of the simulated geometry with a thickness of 250 nm. Thanks to the symmetry, only half of the geometry is considered to speed up the simulation process.

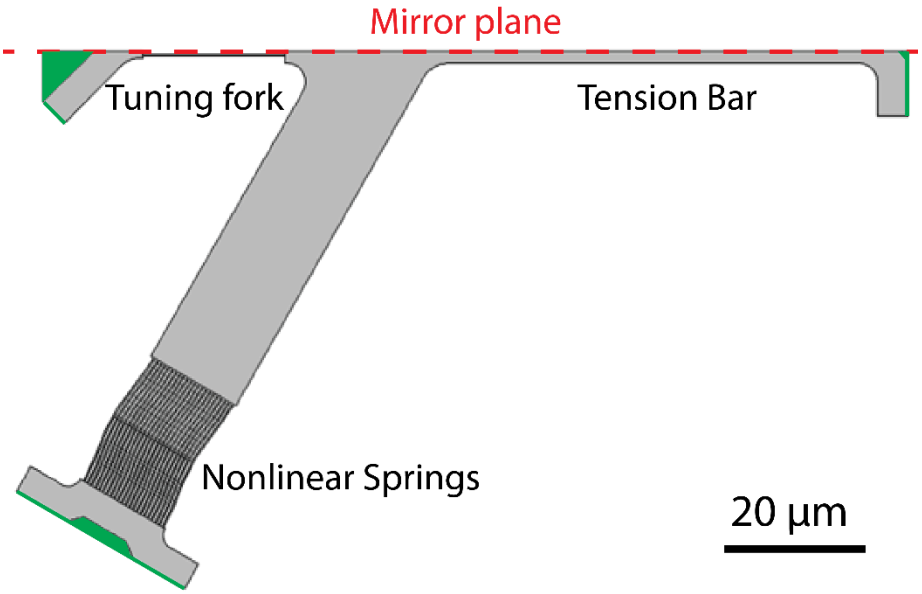

Figure S2 The geometry used in FEM simulation. Only half of the geometry is considered to speed up the process.

The material of the structure is Si_3N_4 with Young's modulus $E \approx 310$ GPa and mass density $\rho \approx 3000$ kg/m^3. The coefficient of thermal expansion (CTE) of the Si substrate is $\approx 2.6\times10^{-6}$ K^{-1} and the Si_3N_4 device layer is $\approx 1.6\times10^{-6}$ K^{-1}.

The used mesh type is the free tetrahedral mesh and the mesh size is with a minimum element size of 0.5 nm. The mesh convergence of the simulation is confirmed.

The physics model is standard and routine. The simulation is done on the solid mechanics module with a pre-stressed analysis interface. The boundary conditions are listed as follows. The initial stress is pre-applied to the whole structure. The boundary labeled by the red dash line is set to be symmetry boundary condition. The green boundaries (anchored on the substrate) are set to be fixed. Other boundaries are set to be free. Next, we solve this stationary problem with the FEM. The solver we used is a MUltifrontal Massively Parallel sparse direct (MUMPS) iterative solver that takes the geometric nonlinearity into account[1]. It covers the geometric

nonlinearity, i.e. the deformed-geometry-based "spring constant". After the system reaches the equilibrium, we extract the tensile stress on the tuning fork. Finally, we numerically solve the pre-stressed eigenvalue (eigenfrequency) problem by FEM using the calculated tensile stress from the previous step[2]. We repeat the above steps and sweep the initial stress applied and obtain Figure 1 (e). Lines with different color corresponds to the different ratios between the width of springs and tension bar.

The stress and frequency variations due to CTE can be analyzed by applying a pre-calculated displacement from CTE on the green boundaries. However, The stress and frequency variations due to CTE are equivalent to variation due to the change in the residual (initial) stress: in a device prior to release the thermal expansion of the substrate results in a change in the thin film stress with a change in temperature. Therefore, we do not repeatedly show temperature analysis again.

Force-displacement relation of the nonlinear springs

The nonlinear springs consist of 22 springs which are 180 nm wide and L = 20 μm long, respectively. The nonlinear springs are curved before undercut with the shape of a period of a cosine function as $A_0\cos(2\pi x/L)$, where A_0 = 0.48 μm, giving the undeformed beam length of approximately $L + \pi^2 \frac{{A_0}^2}{L} \approx 20.11$ μm. Figure S2 (a) presents the top view of the nonlinear springs.

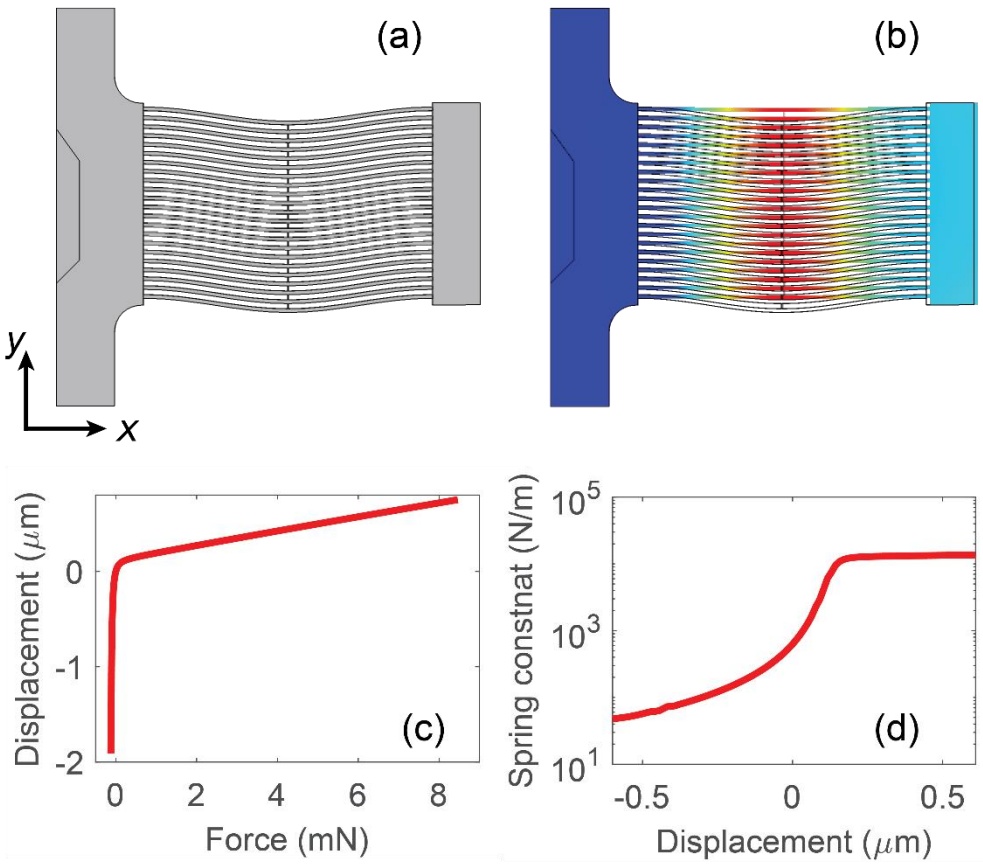

Figure S3 Nonlinear spring simulation. (a) Top view of the nonlinear springs used in the simulation. (b) Total deformation of the nonlinear springs. Colors label the displacement magnitude. (c) Force-displacement curve of the nonlinear springs. (d) Nonlinear spring constant as a function of displacement.

Using FEM, we simulate the force-displacement curve along the *x*-axis shown in Figure S2 (c). By doing a derivative on it, we obtain the nonlinear spring constant as a function of displacement shown as Figure S2 (d). A transition occurs approximately at the displacement of $\pi^2 \frac{{A_0}^2}{L} \approx 0.11$ μm, the difference between the spring length and the initial distance between the spring ends L. Below this displacement the nonlinear springs are not fully straightened. The geometric nonlinearity gives rise to a displacement dependent spring constant. As the springs are fully straightened at ≈ 0.18 μm, the geometric nonlinearity disappears, and the spring constant keeps as a constant, more than an order of magnitude stiffer than the zero-displacement state. Figure S2 (b) shows the simulated total displacement of the springs. The dash lines represent their original position. The center of the springs has the largest lateral displacement in the *y*-direction.

The full system can be usefully understood as a set of connected springs shown in Figure S3. Design of each spring is characterized by its stiffness and the initial (as-fabricated) length. To calculate the behavior upon release, first, the residual stress can be used to calculate the "zero-load" length of each spring, for which the spring would apply zero force. From that zero-load length the springs need to be stretched to meet at an equilibrium point *o*, at which the four springs have to apply a zero net force. As shown in Figure S2, $k_{ns} \approx 0$ until it is stretched by a distance ≈ 0.11 μm, after which the stiffness is constant, comparable to k_{bar} and substantially larger than k_{fork}. The sysem then behaves elastically, with the lengths and stiffnesses (mostly of the tension bar and nonlinear clamps) contloling the location of *o* as a function of stress and/or isotropic stretching of the substrate with the attached anchor points. Compensation is achieved when *o* is moving to the left with increasing tensile stress and/or increasing stretch of the substrate, maintaining a constant stress in the tuning fork.

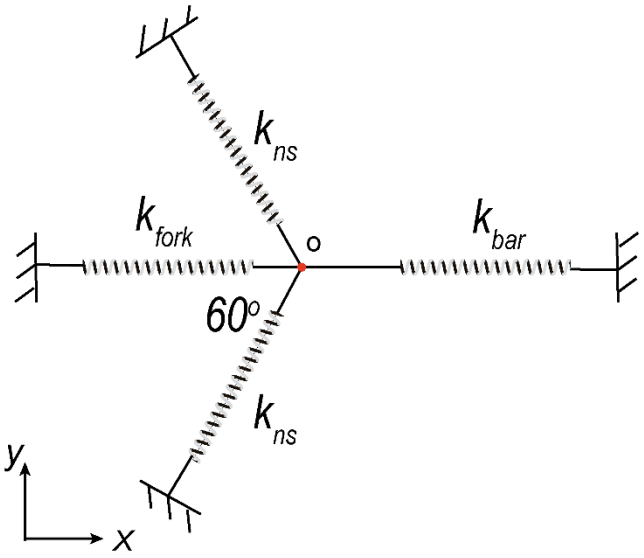

Figure S4 Schematic of the system. k_{ns}**,** k_{fork} **and** k_{bar} **represent the spring constants of nonlinear springs, tuning fork and tension bar, respectively.**

It is noteworthy that although this simple analysis is helpful to qualitatively understand how the compensation works, it is still necessary to do the quantitative complete stress analysis, as shown in the previous section, for obtaining the optimal compensation.

References:

1. What Is Geometric Nonlinearity? *COMSOL Multiphysics* https://www.comsol.com/blogs/what-is-geometric-nonlinearity/.
2. How to Analyze Eigenfrequencies That Change with Temperature. *COMSOL Multiphysics* https://www.comsol.com/blogs/how-to-analyze-eigenfrequencies-that-change-with-temperature/.